

**Grain reconstruction of porous media: Application to a low-porosity Fontainebleau sandstone**J.-F. Thovert,<sup>1</sup> F. Yousefian,<sup>2</sup> P. Spanne,\* C. G. Jacquin,<sup>3,†</sup> and P. M. Adler<sup>2</sup><sup>1</sup>*LCD-PTM, CNRS, SP2MI, Boulevard 3, Teleport 2, BP30179, 86962 Futuroscope Cedex, France*<sup>2</sup>*IPGP, Tour 24, 4 Place Jussieu, 25252 Paris Cedex 05, France*<sup>3</sup>*38 Grand Rue, 86310 Saint Savin, France*

(Received 17 January 2001; published 23 May 2001)

The fundamental issue of reconstructing a porous medium is examined anew in this paper, thanks to a sample of low-porosity Fontainebleau sandstone that has been analyzed by computed microtomography. Various geometric properties are determined on the experimental sample. A statistical property, namely, the probability density of the covering radius, is determined. This is used in order to reconstruct a porous medium by means of a Poissonian generation of polydisperse spheres. In a second part, the properties of the real experimental sample and of the reconstructed one are compared. The most important success of the present reconstruction technique is the fact that the numerical sample percolates despite its low porosity. Moreover, other geometrical features and conductivity are found to be in good agreement.

DOI: 10.1103/PhysRevE.63.061307

PACS number(s): 61.43.Gt

**I. INTRODUCTION**

Thresholded Gaussian field techniques have become a standard tool for the reconstruction of the microstructure of consolidated porous media, and were applied over the past decade to obtain good predictions of the transport properties of many types of materials. An historical account, a description of the implementation and a set of applications are provided by Adler and Thovert [1]. A major advantage of this approach is the absence of any adjustable parameters. The reconstruction is based on statistical geometrical data, namely, the porosity and spatial correlation function, possibly position dependent, which can be measured on real samples by standard image analysis. The most usual implementations make use of moving average or Fourier transform methods to generate the underlying continuous correlated field to be thresholded to obtain the binary phase function with the desired statistical characteristics.

An alternative approach uses simulated annealing to directly generate the phase function, according to the same kind of geometrical conditioning parameters [2–5]. This technique allows one to introduce additional constraints, such as higher order statistical moments, but is computationally much more demanding.

The former techniques are purely geometric, in the sense that they do not attempt to simulate the actual genesis of the porous material. If the microstructure results from known mechanisms, it is appealing to directly incorporate this knowledge in the simulation procedure. For instance, sedimentary rocks result from the deposition of grains followed by a consolidation, due to various diagenetic processes. Despite the consolidation, the underlying grain packing structure may still be visible. Hence, another class of reconstruction procedures consists in the simulation of the generating processes, i.e., of the primary grain sedimentation followed by diagenetic processes such as compaction and cementa-

tion. The first step can be achieved, for monodisperse or polydisperse grain size distributions, e.g., by using the numerical tools developed by Coelho *et al.* [6]. The second step requires additional information, relative to the kinetics of the consolidation process, which determines the final morphology of the pore space. Øren *et al.* [7], Biswal *et al.* [8] and Øren and Bakke [9] describe such a model, which includes various consolidation mechanisms, with several fitting parameters.

The purpose of this paper is to present a reconstruction technique, which introduces an underlying granular structure, but only makes use of geometrical parameters that can be measured on images of real samples. From this stand point, the methodological approach is the same as for the correlation technique; all geometrical quantities are measured and a medium is generated with the same statistical characteristics. This technique is based on a Poissonian penetrable sphere model, conditioned by the experimental solid size distribution. Thus, the size distribution of the solid phase should be quantified in the first place, and a sizing technique that provides the required information is introduced. These techniques are applied to the analysis of a low-porosity Fontainebleau sandstone sample, based on a high-resolution three-dimensional digital image obtained by x-ray computed microtomography (CMT). First, the geometry and the transport properties of the real sample were thoroughly characterized. Then, the same analysis was repeated on a numerically reconstructed sample, which allows a direct assessment of the merit of the reconstruction algorithm, with respect to a variety of geometrical and transport-related criteria. Special emphasis is put on the quantification of local variability in the real material, and on its rendering in the reconstructed one.

This paper is organized as follows. The first three sections are devoted to a general description of the methods. The geometrical characterization tools used in this study are presented in Sec. II. This includes the first two statistical moments of the phase function, i.e., porosity and autocorrelation function, and the solid size distribution, which is used for

\*Deceased.

†Retired.

conditioning the reconstruction procedure. Other geometrical characteristics, such as the skeleton of the pore space are used to compare the properties of the real and reconstructed samples. The reconstruction procedure is described in Sec. III. The methods of solution for the transport properties, namely, percolation and conduction, are presented in Sec. IV.

The rest of the paper describes an application of these characterization and reconstruction tools. A thorough description of the experimental sample is given in Sec. V. The CMT data are described, and the rock geometrical and transport properties are examined. Spatial heterogeneity is investigated by considering the various properties at different scales. The same analysis is conducted in Sec. VI on a numerically reconstructed sample. A systematic comparison is made with the data directly obtained from the CMT image.

Finally, the main results are summarized in Sec. VII.

## II. GEOMETRICAL CHARACTERIZATION OF A POROUS MATERIAL

### A. The phase function and its statistical moments

The microstructure of a porous medium can be fully described by the phase function  $Z$

$$Z(\mathbf{x}) = \begin{cases} 1 & \text{if } \mathbf{x} \text{ belongs to the pore space} \\ 0 & \text{otherwise,} \end{cases} \quad (1)$$

where  $\mathbf{x}$  denotes the position with respect to an arbitrary origin. In most practical cases,  $Z$  is known from two- or three-dimensional binary digital images, made of pixels or voxels with size  $p_x$ , or given in the elementary cubes with size  $a$  that constitute reconstructed numerical samples. The phase function is then defined at discrete locations  $\mathbf{x}$ , corresponding to the positions of these elementary volumes, which are assumed to be entirely filled with either phase, void or solid.

In view of the random character of most real materials, it is quite natural to describe the phase function  $Z$  by its statistical moments. The porosity  $\epsilon$  and the spatial correlation  $R_Z(\mathbf{u})$  can be defined by the statistical averages (which are denoted by brackets  $\langle \cdot \rangle$ )

$$\epsilon = \langle Z(\mathbf{x}) \rangle, \quad (2)$$

$$R_Z(\mathbf{u}) = \frac{\langle [Z(\mathbf{x}) - \langle Z \rangle][Z(\mathbf{x} + \mathbf{u}) - \langle Z \rangle] \rangle}{\epsilon(1 - \epsilon)}. \quad (3)$$

For homogeneous and isotropic materials,  $R_Z$  is a function of the modulus of the lag  $u = \|\mathbf{u}\|$  only,  $R_Z(\mathbf{u}) = R_Z(u)$ . Notice that  $\epsilon(1 - \epsilon)$  in Eq. (3) equals the variance  $\sigma_Z^2$  since  $Z^2(\mathbf{x}) = Z(\mathbf{x})$ . A characteristic length scale of the microstructure is provided by the correlation length  $\mathcal{L}$ , which is defined as the integral of the correlation function

$$\mathcal{L} = \int_0^\infty R_Z(u) du. \quad (4)$$

In anisotropic media, the correlations for  $\mathbf{u}$  parallel to the  $x$ ,  $y$ , and  $z$  axes are denoted  $R_{Zx}$ ,  $R_{Zy}$ , and  $R_{Zz}$ , respectively.

In heterogeneous media, the statistical moments of the phase functions can be position dependent. In particular, regional variations of the first moment may exist. A position-dependent porosity field  $\bar{\epsilon}(\mathbf{r})$  can be defined as the local average  $\langle Z \rangle_\Omega$  of the phase function  $Z$  over domains  $\Omega$  of arbitrary size  $L$  centered at  $\mathbf{r}$ . The statistical distribution of this field can be quantified, as well as the variance  $\sigma_\epsilon^2$  and spatial correlation  $C_\epsilon^-(\mathbf{u})$

$$\sigma_\epsilon^2 = \langle (\bar{\epsilon} - \epsilon)^2 \rangle, \quad (5a)$$

$$C_\epsilon^-(\mathbf{u}) = \langle [\bar{\epsilon}(\mathbf{r}) - \epsilon][\bar{\epsilon}(\mathbf{r} + \mathbf{u}) - \epsilon] \rangle. \quad (5b)$$

The brackets  $\langle \cdot \rangle$  denote here an averaging over the position  $\mathbf{r}$ , and  $\epsilon$  is the overall mean porosity  $\epsilon = \langle Z \rangle = \langle \bar{\epsilon}(\mathbf{r}) \rangle$ . These quantities can possibly be used to condition subsequent reconstructions of heterogeneous media.

In addition, they can be analyzed as functions of the averaging domain size  $L$ . The local porosity theory makes use of local porosity and local percolation probability distributions, either to predict macroscopic transport properties [10], or as a reference criterion for the assessment of pore-space models [11,12], as done here in Secs. V and VI.

### B. Solid size distribution

Sandstones are sedimentary rocks, which result from deposition of quartz grains followed by consolidation. For instance, an underlying grain-packing structure is still clearly visible in Fig. 1, despite a strong consolidation. It is tempting to use this feature as the starting point for the reconstruction procedure. Thus, the size distribution of the solid phase should be quantified, in order to condition the reconstructed samples.

Of course, the primary constitutive grains are not directly visible on binary images due to cementation. It is not our purpose, however, to identify the primary grains and the cement, in order to successively simulate the grain deposition and the subsequent diagenetic processes. Instead, we look for a description of the solid size distribution, which could be used in a purely geometrical simulation procedure to mimic the microstructure of experimental granular samples, regardless of their genesis.

A sizing technique that provides such information is described in this section. It is based on classical mathematical morphology concepts. The theoretical background is given in details by Matheron [13] and Serra [14]. A simple introduction to some of the basic concepts used here is also provided by Horgan [15]. Thus, the novelty does not lie in the mathematical apparatus, but rather in its actual implementation for two- or three-dimensional images of rocks, and in its subsequent use in a reconstruction procedure, in order to render specific features of the real material.

We will define here the covering radius  $r_c$  for each point in the solid phase of a porous medium, which corresponds in mathematical morphology to a sizing by openings. The following presentation is kept as simple as possible. In particu-

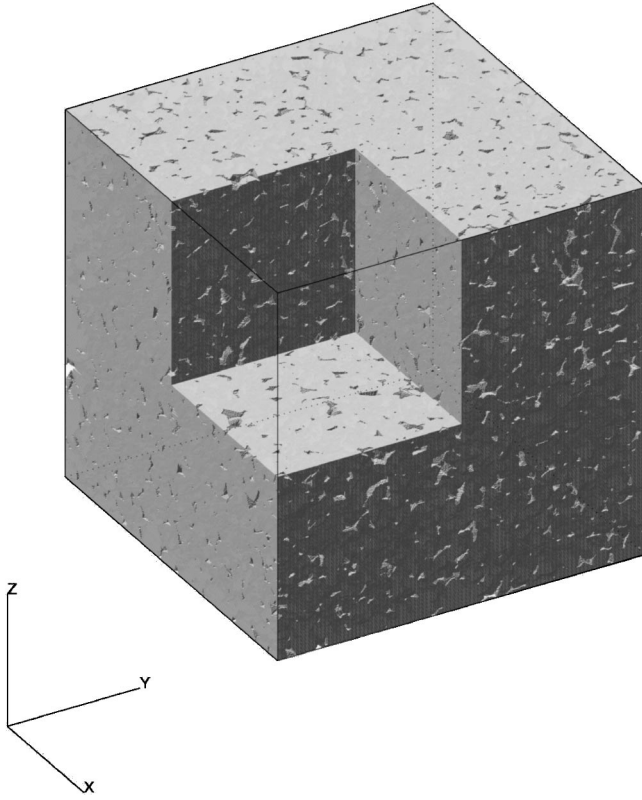


FIG. 1. Three-dimensional view of the CMT image of the experimental sample. The dimensions are  $512^3$  voxels, i.e.,  $(3.23 \text{ mm})^3$ .

lar, we always suppose that the structuring element  $B$  is a ball (disk or sphere), although all the following is also valid for squares or cubes, which may be, sometimes, of interest. The three references above provide the general formulas for other shapes of  $B$ .

The dilation of the domain  $A$  (representing here the solid phase) by a structuring element  $B_\lambda$  (here a ball with radius  $\lambda$ ) is the set  $A \oplus B_\lambda$  covered by all the translations of  $B_\lambda$  centered in  $A$

$$A \oplus B_\lambda = \bigcup_{\mathbf{r} \in A, \mathbf{s} \in B_\lambda} (\mathbf{r} + \mathbf{s}). \quad (6)$$

The erosion is the dual operation, corresponding to the dilation of the complementary  $A^c$  of  $A$ . It corresponds to all points in  $A$  not covered by a ball  $B_\lambda$  centered out of  $A$

$$A \ominus B_\lambda = (A^c \oplus B_\lambda)^c. \quad (7)$$

It can also be viewed as the locus of the centers of the translations of  $B_\lambda$  entirely contained in  $A$ . The opening  $A_{B_\lambda}$  (or in short  $A_\lambda$ ) by  $B_\lambda$  is the result of an erosion followed by a dilation

$$A_{B_\lambda} = A_\lambda = (A^c \ominus B_\lambda) \oplus B_\lambda. \quad (8)$$

The main effects of an erosion are to shrink the size of  $A$ , and to remove its components that are too small to contain  $B_\lambda$ . Conversely, a dilation increases the size of  $A$ , fills small inner holes and possibly connects components of  $A$  separated

by a narrow gap. Finally, an opening filters out small concavities from the contour, but keeps the concavities and removes the small parts of  $A$ .

The main property of  $A_\lambda$  for our purposes is that  $A_\lambda$  is the set of points in  $A$  that can be covered by a ball of radius  $\lambda$  contained in  $A$ . A size  $r_c(\mathbf{r})$  can be associated with any point in  $A$ , defined as the radius of the largest ball contained in  $A$  that covers  $\mathbf{r}$ . In other words

$$r_c(\mathbf{r}) = \sup\{\lambda : \mathbf{r} \in A_\lambda\}, \quad (9a)$$

$$A_\lambda = \{\mathbf{r} \in A : r_c(\mathbf{r}) \geq \lambda\}. \quad (9b)$$

We denote  $r_c(\mathbf{r})$  as the covering radius of  $\mathbf{r}$ . It corresponds to the size  $\lambda_A(\mathbf{r})$  in Ref. [14] (Chapter X). It is equal to zero out of  $A$ , i.e., in the pore space.

Note that  $r_c(\mathbf{r})$  is not directly related to the distance  $d_I(\mathbf{r})$  from  $\mathbf{r}$  to the closest point on the boundary of  $A$ , except for the property  $d_I \leq r_c$ . For instance, all points in a sphere with radius  $\Lambda$  have a covering radius  $r_c = \Lambda$ .

A solid size distribution can be defined from the distribution function  $G$  of the pointwise size  $r_c$ ,

$$G(R) = (\text{Volume fraction of the set})\{\mathbf{r} \in A ; r_c(\mathbf{r}) < R\} \quad (10a)$$

$$= 1 - (\text{Volume fraction of } A_\lambda). \quad (10b)$$

It is generally defined relative to the volume of  $A$ . For convenience, we use here absolute volume fraction, relative to the whole porous medium volume, with

$$G(0) = (\text{porosity}), \quad G(+\infty) = 1. \quad (11)$$

The probability density function  $g(R)$  deduced from  $G$  contains at least one Dirac contribution  $\varepsilon \delta(0)$ , and possibly others, if part of the solid consists of spherical grains.

Given a three-dimensional digital image of a porous medium, the covering radii  $r_c$ , and thus the family of domains  $A_\lambda$  and the functions  $g$  and  $G$  are easily obtained by elementary numerical analysis. Of course, the structuring element  $B_\lambda$  is then the discrete version of a ball with radius  $\lambda$  on the underlying lattice. Since squared distances between pixels are integer numbers, in lattice units,  $r_c^2$  is always integer.

The determination of the three-dimensional solid size distribution from two-dimensional images is a more difficult stereological problem that is not addressed at this stage.

The probability density function  $g(R)$  can be viewed as a three-dimensional extension of the lineal-path function  $L(z)$ , defined by Lu and Torquato [16] as the probability that a line segment of length  $z$  is fully in one of the phases, when randomly thrown into the sample. This function was evaluated by Quintanilla and Torquato [17] for Poissonian disks and spheres, and actually used by Yeong and Torquato [3] as the conditioning criterion for a simulated annealing reconstruction procedure.

### C. Topology, skeleton of the pore space

The connectivity of the pore space can be characterized by the cyclomatic number (or genus)  $\beta_1$ , which is equal to

the number of independent cycles in its associated graph. This graph, represented by the skeleton of the pore space [14], can be viewed as a simplified image of the pore space, analogous to a capillary network. It is determined by a progressive conditional thinning algorithm [18]. The cyclomatic number is equal to

$$\beta_1 = m - n + 1 \quad (12)$$

where  $m$  and  $n$  are the number of edges and vertices in the graph, respectively. The volumetric number of cycles per unit volume is denoted by  $\beta'_1$ .

Various statistical quantities can be measured on the skeleton. Let  $d_s$  denote the distance of a point on the skeleton to the closest solid. Its minimum  $r_e$  along the edge  $e$  is the critical radius of this edge, i.e., the radius of the largest sphere that can travel along  $e$ . The radius  $r_M$  of the largest cavity in the sample (radius of the largest sphere that can fit into the pore space) is also readily available.

More generally, statistics relative to the elements of the skeleton can be evaluated; averages, standard deviations and histograms of the radii  $r_e$  or of the end-points distance  $d_e$  of the edges ( $e = 1, 2, \dots, m$ ), of the radii  $r_v$  and coordination number  $z_v$  (number of incident edges) of the vertices ( $v = 1, 2, \dots, n$ ), volumetric number  $N'_v$  of vertices, and mean coordination number  $\bar{z}_v$  that is related to the mean number of cycles per vertex  $\beta'_1/N'_v$  by

$$\frac{\beta'_1}{N'_v} = \frac{\bar{z}_v}{2} - 1 - \frac{1}{n} \approx \frac{\bar{z}_v}{2} - 1 \quad (n \gg 1). \quad (13)$$

The correlations of these quantities can also be quantified, by the covariance  $C_{ee}$  of the radii of adjacent edges, the covariance  $C_{ev}$  of the radii of adjacent edge/vertex couples and the covariance  $C_{el}$  of the radius and end-points distance of edges, which are defined as

$$C_{ee} = \frac{\langle (r_{e'} - \bar{r}_e)(r_{e''} - \bar{r}_e) \rangle}{\sigma_{r_e}^2}, \quad (14a)$$

$$C_{ev} = \frac{\langle (r_e - \bar{r}_e)(r_v - \bar{r}_v) \rangle}{\sigma_{r_e} \sigma_{r_v}}, \quad (14b)$$

$$C_{el} = \frac{\langle (r_e - \bar{r}_e)(d_e - \bar{d}_e) \rangle}{\sigma_{r_e} \sigma_{d_e}}. \quad (14c)$$

The indices  $e'$  and  $e''$  in Eq. (14a) refer to edges with a common vertex. The average in Eq. (14b) is taken over the pairs of connected edges  $e$  and vertices  $v$ .

It should be kept in mind that the quantities introduced in this paragraph are measured on the mathematical skeleton, which may differ quite significantly from an intuitive pore/throat vision of the pore space. Besides, some of these quantities such as  $N'_v$  and  $\bar{z}_v$  depend on the resolution of the discretization for the calculations (see the discussion by Bekri *et al.* [19]). However, the cyclomatic numbers  $\beta_1$  and  $\beta'_1$  are unaffected by a change in spatial discretization, pro-

vided, of course, that resolution is good enough to preserve the pores. In addition, the skeletons determined in the following for the experimental and reconstructed samples are obtained for exactly identical resolutions, thereby allowing meaningful comparisons.

The statistics of the skeleton elements may prove useful for other simulation purposes, for instance to provide capillary network models of the porous material with statistical informations on pore diameters, coordination numbers and so on. In this paper, they are only used as an additional criterion for the comparison of the real and reconstructed media.

### III. RECONSTRUCTION PROCEDURE

We describe in this section a Poissonian penetrable sphere model, conditioned by the experimental solid size distribution. In the present implementation, the model belongs to the general class of the so-called Boolean models. Recall that Boolean models are stationary Poisson processes, where the size and shape of the inserted objects can be randomized, but with a probability law identical for all objects and independent of their position [20]. However, it is conceptually easy to generalize the model by introducing regional variations of the porosity or of the solid size distribution, thereby loosing the Boolean character.

General descriptions of the properties of penetrable sphere models are provided by Hall [20] and Torquato and co-workers (see, e.g., [21] and references therein).

Consider first the case of monodisperse grains. The porosity is directly related to the number density  $\rho_p$  of grains with volume  $V_p$  per unit volume

$$\epsilon = e^{-\mu_p}, \quad \mu_p = \rho_p V_p. \quad (15)$$

The correlation function is given by

$$R_Z(u) = \frac{\epsilon^{1+3u'/4-u'^3/16} - \epsilon^2}{\epsilon(1-\epsilon)} \quad \left( u' = \frac{u}{R_p} \leq 2 \right); \quad (16)$$

$$R_Z(u) = 0 \quad (u \geq 2R_p)$$

where  $R_p$  is the grain radius. Obviously, monodisperse spheres allow to match a single scalar parameter of the real medium to simulate, e.g., the initial slope of the correlation function, which is proportional to the volumetric wetted area [22].

Polydisperse penetrable spheres are required in order to incorporate more morphological information. Such an approach was applied by Glasbey *et al.* [23], but with an *a priori* model for the grain size distribution, whereas this distribution is directly deduced here from measurements on the real sample.

First note that the correlation function of a porous medium resulting from the superposition of penetrable spheres, with a radius probability density  $f(R)$  (in number of grains) can be evaluated analytically [24]. It is given by

$$R_Z(u) = \frac{\epsilon^{\alpha(u)} - \epsilon^2}{\epsilon(1 - \epsilon)} \quad (17)$$

with

$$\begin{aligned} \alpha(u) &= 1 + \frac{3 \langle R^2 \rangle}{4 \langle R^3 \rangle} u - \frac{u^3}{16 \langle R^3 \rangle} + \frac{1}{\langle R^3 \rangle} \\ &\times \int_0^{u/2} \left[ R^3 - \frac{3R^2 u}{4} + \frac{u^3}{16} \right] f(R) dR, \quad (18a) \\ &= 2 - \frac{1}{\langle R^3 \rangle} \int_{u/2}^{+\infty} \left[ R^3 - \frac{3R^2 u}{4} + \frac{u^3}{16} \right] f(R) dR. \quad (18b) \end{aligned}$$

Equations (17) and (18) can be inverted, to determine  $f(R)$  from the correlation function  $R_Z$ , provided, of course, that the medium actually corresponds to penetrable solid spheres. The inversion formula and the necessary criterion on  $R_Z$  are given in the Appendix. Unfortunately, the inversion is strongly affected even by small violations of this criterion. In addition it is very sensitive to statistical noise in the long-range part of the correlation function. Therefore, we apply in practice the alternative technique described below, based on the solid size distribution spectrum introduced in Sec. II B. It always yields a distribution  $f(R)$  that allows to mimic the solid size distribution in the real medium, even though its solid phase is not likely to be made up of penetrable spheres, and it is less sensitive to statistical fluctuations.

It has been shown in Sec. II B how the covering radius  $r_c(\mathbf{r})$ , i.e., the radius of the largest sphere entirely lying in the solid and covering  $\mathbf{r}$ , can be determined for any point  $\mathbf{r}$  in the solid phase. The sphere size distribution  $f(R)$  will be determined from the probability density  $g$  and the distribution function  $G$  of the covering radius

$$g(r) dr = \text{Volume fraction of points with } r \leq r_c < r + dr, \quad (19a)$$

$$G(r) dr = \int_0^r g(s) ds = \text{Volume fraction of points with } r_c < r. \quad (19b)$$

Obviously, many spheres will be partially or totally masked by larger ones [see Fig. 2(a)]. The radius  $r_c$  in the overlaps is then equal to the largest radius ( $R_1$  in the Figure). Conversely, the radius  $r_c$  in the largest sphere in Fig. 2(a) is unaffected by the presence of the smaller ones. We make here the approximation that situations like Fig. 2b are statistically negligible. In order to modify  $r_c$  in the large sphere to  $R'_1 > R_1$ , it is required that it is totally surrounded by a continuous shell of smaller ones, which is unlikely for large grains, especially in three dimensions. This is subject to *a posteriori* verification, and indeed in the present application, the covering radius spectrum in the reconstructed media differs only slightly from the prescribed spectrum, with a bias towards larger radii. It should be noted however that the

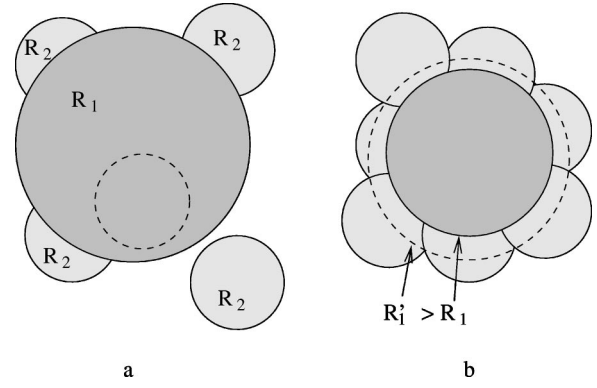


FIG. 2. Poissonian spheres (two-dimensional illustration). The covering radius  $r_c$  in the whole dark sphere in (a) is equal to its radius  $R_1$ . Situations like (b) where a continuous shell of grains increases  $r_c$  to  $R'_1 > R_1$  are ignored.

simulated material has a very low porosity, about 0.07, which is the worst situation in this respect. This artifact is almost totally eliminated with larger void fractions, as shown by Yousefian *et al.* [25], who consider a sandstone of porosity 0.17.

These remarks provide the key for the determination of the amount of grains of each size to be inserted. The largest spheres must simply match the volume fraction of the maximal value of  $r_c$ . Then, the amount of smaller spheres is determined from the volume fraction  $g(R)$ , corrected for the masking effect of the larger ones, i.e.,  $g(R)/G(R)$ . Denote  $\mu(R)$  the volumetric density of spheres with radius  $R$  [see Eq. (15)]

$$\mu(R) = \rho(R) V(R), \quad (20a)$$

$$\begin{aligned} \rho(R) dR &= \text{Number of spheres per unit volume} \\ &\text{with radius in } [R, R + dR] \quad (20b) \end{aligned}$$

with  $V(R) = 4/3 \pi R^3$ . Then, the number  $\rho(R)$  of spheres of size  $R$  to be inserted per unit volume is directly obtained by

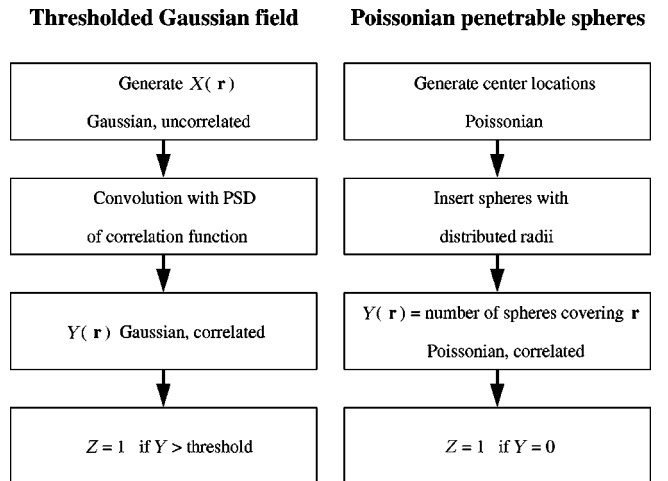


FIG. 3. Main steps of the penetrable Poissonian spheres and thresholded Gaussian field reconstructed procedures.

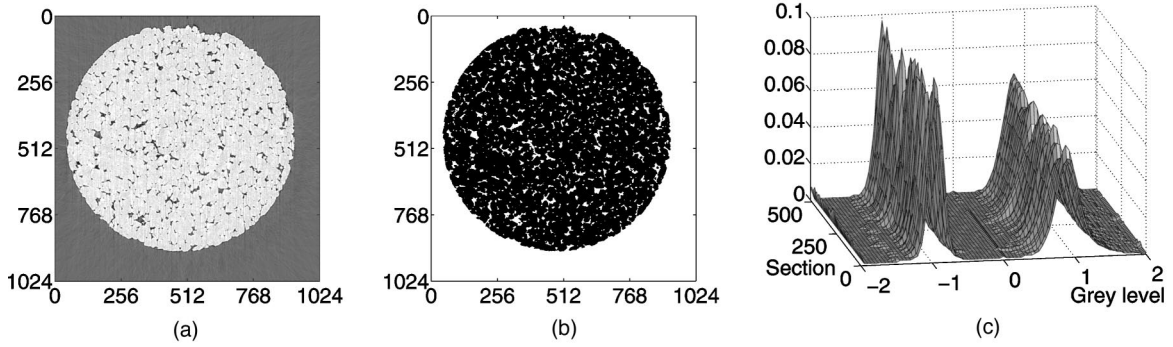


FIG. 4. Examples of gray level (a) and binarized (b) images of a section through the Fontainebleau sandstone sample. The histogram of the gray levels in the whole  $513 \times 1023 \times 1023$  voxels CMT image (c). The gray levels in (c) are centered and normalized by the global mean and standard deviation.

$$\mu(R) = \frac{g(R)}{G(R)}, \quad \rho(R) = \frac{1}{V(R)} \frac{g(R)}{G(R)}. \quad (21)$$

It is interesting to note that although a counterpart of the covering radius  $r_c$  can be straightforwardly defined in the void phase, it probably cannot be used for the present purpose of determining  $f(R)$ . Hall [20] has shown that for poly-disperse Poissonian disks in the plane, the statistical distribution of the first contact distance, i.e., the distance  $d_s$  from a point in the pore space to the closest solid, only depends on the mean disk perimeter and area, whereas the distribution of  $d_I(\mathbf{r})$  is more complex.

A parallel can be made between the Poissonian penetrable sphere model and the thresholded Gaussian field reconstruction procedure, as illustrated in Fig. 3. Recall that the thresholded field technique [26] consists in the following steps. First generate a random uncorrelated Gaussian field,  $X(\mathbf{r})$ . Convolve it with a kernel derived from the correlation function  $R_Z$  to obtain a correlated Gaussian field  $Y(\mathbf{r})$ . Finally, the phase function  $Z(\mathbf{r})$  is equal to 1 where  $Y$  exceeds a threshold that depends on the target porosity.

The generation of the grain center locations corresponds to the generation of the initial random field  $X$ . Then, spheres with a prescribed size distribution are inserted and a Poissonian correlated field  $Y(\mathbf{r})$  can be defined as the number of spheres covering  $\mathbf{r}$ ; finally, the phase function  $Z$  is again obtained by thresholding  $Y$ . In both cases, the definition of  $Y$  incorporates the same type of geometrical information derived from the experimental porosity and spatial correlations.

The main difference is that only a certain class of correlation functions can be generated with the Poissonian model, whereas no such limitation exists with the Gaussian field technique.

The penetrable sphere model can also be regarded as a variant of the generating technique of Di Federico and Neuman [27], who also superpose uncorrelated fields with identical correlation functions within a change of scale. Only the shape of this correlation is different, given here by Eq. (16), instead of a Gaussian or exponential function.

Both the thresholded Gaussian field and the Boolean methods offer no control over the statistical moments of the phase function, beyond their mean and two-point correlation.

Higher-order moments, such as three- and four-point correlations, are determined by the reconstruction procedure, and may differ in the Poissonian and Gaussian models. This point is not addressed in the present paper, but the three- and four-point correlations in a real sandstone and in porous media reconstructed by using both the penetrable spheres and thresholded Gaussian fields techniques are systematically compared by Yousefian *et al.* [25].

#### IV. MACROSCOPIC PROPERTIES: METHODS OF SOLUTION

We show in this section how some of the macroscopic properties of porous media can be numerically determined [26].

##### A. Percolation

The first property to be determined is whether the pore space in the material percolates or not, i.e., whether a continuous path through the pore space exists between two opposite faces of the sample. In the absence of percolation, all the macroscopic coefficients for transport processes in the pore space are trivially zero.

Unless otherwise stated, we considered only percolation along a single direction, corresponding to the  $x$  axis. Hence, a sample is said to percolate when its two opposite faces normal to this direction can be connected through the pore space; this corresponds to the rule  $R_1$  as defined by Reynolds *et al.* [28]. The percolation status of the samples was checked by use of a pseudodiffusion algorithm, as described by Thovert *et al.* [18].

##### B. Conductivity

At the macroscopic scale, an isotropic porous medium can be characterized by a macroscopic conductivity coefficient  $\bar{D}$ , which only depends on its microstructure. When the pore space is filled by a conducting fluid of conductivity  $\sigma_0$ , the porous medium has an effective conductivity  $\sigma_0 \bar{D}$ . The electrical terminology is used here but the following developments are also valid for thermal conduction and for diffusion of particles whose size is small with respect to a typical pore size.

In order to determine  $\bar{D}$ , one has to solve Laplace's equation

$$\nabla^2 T = 0, \quad (22)$$

where  $T$  is the potential field, together with the no-flux boundary condition at the surface of the solid  $S_p$ , when the solid phase is assumed to be insulating

$$\mathbf{m} \cdot \nabla T = 0, \quad \text{on } S_p, \quad (23)$$

where  $\mathbf{m}$  is the unit normal vector to  $S_p$ . This hypothesis of insulating solid phase is well verified for sandstones. The Neumann problem (22) and (23) is solved via a second-order finite-difference formulation, by use of a conjugate-gradient method [29].

We determine the conductivity coefficient  $\bar{D}$  along the  $x$  direction, by imposing constant potentials at the upstream and downstream faces of the sample, and no-flux conditions on the four other faces.  $\bar{D}$  is obtained from

$$\frac{Q}{S} = -\sigma_0 \bar{D} \frac{\Delta T}{\Delta x}, \quad (24)$$

where  $Q$  is the total flux,  $S$  is the sample cross-section area and  $\Delta T$  is the potential jump.

## V. ANALYSIS OF THE EXPERIMENTAL SAMPLE

This section is devoted to a thorough characterization of the geometrical and transport properties of the experimental sample. The rock under consideration is a low-porosity Fontainebleau sandstone. The acquisition of a digital three-dimensional image by x-ray CMT and part of the subsequent analysis have been presented by Thovert *et al.* [30].

### A. CMT data

A piece of a cylindrical plug, 5.4 mm in diameter, was imaged at ESRF (Grenoble) by x-ray CMT. Gray level images of 513 serial slices were obtained, made up of  $1023 \times 1023$  pixels, of size  $p_x = 6.3 \mu\text{m}$ . These images were easily and unambiguously binarized, thanks to a clearly bimodal distribution of the gray levels (see Fig. 4).

A parallelepipedic subsample was cut from this image, with dimensions  $512^3$  voxels, i.e.,  $(3.23 \text{ mm})^3$ ; it is entirely contained in the core. A three-dimensional visualization of the investigated subsample is provided in Fig. 1. In the following, the  $x$  and  $y$  axes are contained in the slice planes, whereas the  $z$  axis refers to the direction normal to the slices.

### B. Geometrical characterization

#### 1. Global geometrical measurements

Porosity was measured in  $512 \times 512$  sections through the sample, along the  $x$ ,  $y$ , and  $z$  directions. The corresponding profiles are plotted in Fig. 5. No definite trend is observed along the  $x$  and  $y$  axes. The surface-averaged porosity variations around the global average are of the order of 1%. In the  $z$  direction, i.e., along the axis of the plug, a change in po-

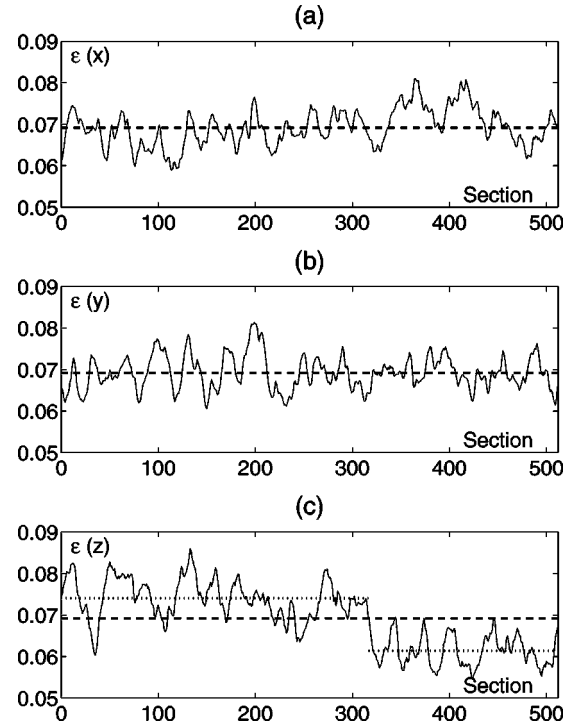


FIG. 5. Porosity profiles  $\epsilon(x)$  (a),  $\epsilon(y)$  (b), and  $\epsilon(z)$  (c) in  $512 \times 512$  voxels sections normal to the coordinate axes, in the experimental sample. The broken lines are the overall average over the  $512^3$  volume. The dotted lines in (c) are separate averages over the 316 first or 196 last sections.

rosity seems to take place around section 316. The mean porosities on either sides differ by about 0.01. The porosity measured in the whole retained sample volume is  $\epsilon = 0.0692$ .

The correlation functions  $R_{Zx}$ ,  $R_{Zy}$ , and  $R_{Zz}$  along the three axes have also been measured in  $(x,y)$ ,  $(x,z)$ , and  $(y,z)$  sections. No significant variations exist, as shown by the example in Fig. 6, where  $R_{Zx}$  measured in successive  $(x,y)$  sections is plotted versus the lag.

The correlations  $R_{Zx}$ ,  $R_{Zy}$ , and  $R_{Zz}$  averaged over the whole volume are displayed in Fig. 7, in Cartesian and semi-

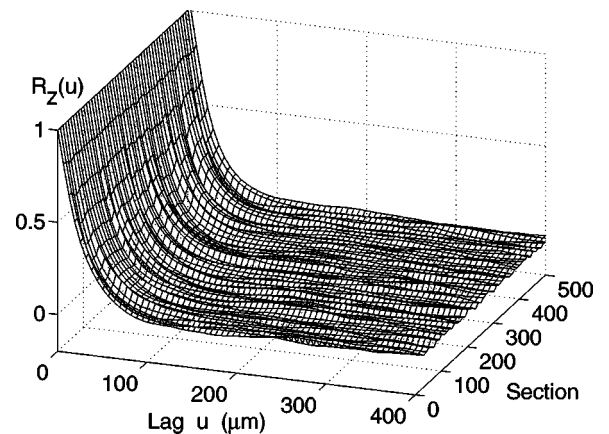


FIG. 6. Correlation function  $R_{Zx}$  measured in successive  $(x,y)$  sections through the experimental sample.

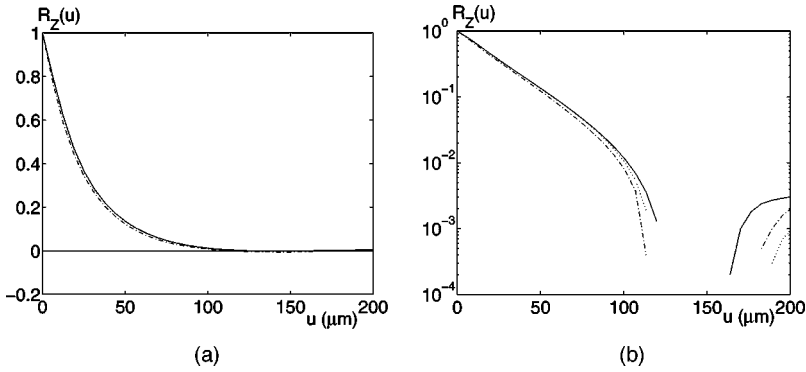


FIG. 7. Correlation functions along the directions  $x$  (—),  $y$  (····) and  $z$  (---) in the experimental sample, versus the lag in microns, in Cartesian (a) and semilogarithmic (b) coordinates.

logarithmic scales. The material appears to be slightly anisotropic.  $R_{Zx}$  and  $R_{Zy}$  are identical, but  $R_{Zz}$  decreases slightly faster. The correlation lengths  $\mathcal{L}_x$  and  $\mathcal{L}_y$  are larger than  $\mathcal{L}_z$  by about 4% (see Table I).

The semilogarithmic plot in Fig. 7 shows that the correlation functions are well described by a negative exponential up to a distance of about 100  $\mu\text{m}$  where  $R_Z$  becomes smaller than  $10^{-2}$

$$R_Z(u) = e^{-u/\lambda}, \quad u < 100 \mu\text{m}. \quad (25)$$

The decay lengths  $\lambda$ , obtained by a least-square fit over the data for lags up to 12 pixel sizes (75  $\mu\text{m}$ ), are given in Table I. They are in good agreement with the corresponding lengths  $\mathcal{L}$ . For longer lags, a slight anticorrelation exists in the range 120–170  $\mu\text{m}$ ; this is a reminiscence of the impenetrability of the constitutive quartz grains, blurred by their size polydispersity and by consolidation. Then,  $R_Z$  randomly fluctuates beyond 200  $\mu\text{m}$ , with a magnitude of the order of  $10^{-2}$  or less.

## 2. Multiscale analysis

Regional porosity variations were studied by considering cubic subsamples  $\Omega$  of varying size. The  $512^3$  complete sample was split into  $N_b$  disjoint blocks containing  $N_c^3$  voxels, with  $N_c$  ranging from 16 to 256. Thus, the block size  $L = N_c p_x$  ranges from 100  $\mu\text{m}$  to 1.6 mm. It is always significantly larger than the correlation lengths  $\mathcal{L}$  or  $\lambda$  in Table I.

The statistical distribution of the decimal logarithm of the porosity  $\bar{\epsilon}$  in individual blocks is displayed in Fig. 8, for various block sizes. As expected, all the distributions become narrower when  $N_c$  increases.

For the smallest blocks ( $N_c = 16$ ), a significant proportion of the blocks (4.9%) contains only solid. As soon as  $N_c \geq 32$ , the probability of zero porosity vanishes, and the porosity distributions look fairly lognormal, as shown by the

TABLE I. Correlation lengths  $\mathcal{L}_x$ ,  $\mathcal{L}_y$ , and  $\mathcal{L}_z$  in the experimental sample, and decay lengths  $\lambda$  in Eq. (25).

	$x$	$y$	$z$
$\mathcal{L}$ ( $\mu\text{m}$ )	24.8	24.6	23.7
$\lambda$ ( $\mu\text{m}$ )	24.9	24.4	23.6

comparison in Fig. 9(a) for  $N_c = 32, 64,$  and  $128$ . The distribution function  $F(y)$  of  $y = \ln(\bar{\epsilon})$  is plotted as a function of the Gaussian distribution function  $G_{\langle y \rangle, \sigma_y}$

$$G_{\langle y \rangle, \sigma_y}(y) = \frac{1}{2} \left[ 1 + \operatorname{erf} \left( \frac{y - \langle y \rangle}{\sqrt{2} \sigma_y} \right) \right], \quad (26)$$

where  $\langle y \rangle$  and  $\sigma_y$  are the mean and standard deviation of  $y$ , for each block size. The three curves are close to the first diagonal, which corresponds to a perfect fit by the lognormal law.

The local porosity standard deviation  $\sigma_{\bar{\epsilon}}$  is given in Table II. It is plotted versus the measuring block size in Fig. 10. Note that the statistics are constrained by the finite size of the

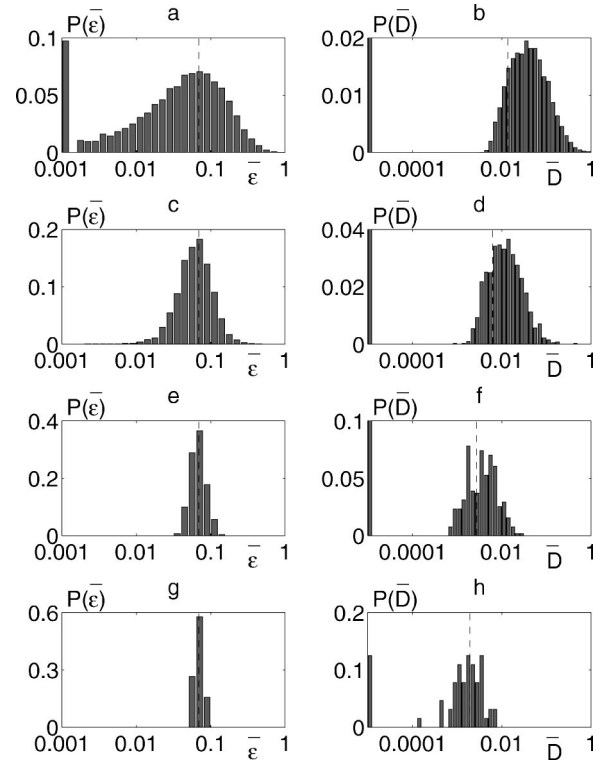


FIG. 8. Histograms of the decimal logarithms of the porosity  $\bar{\epsilon}$  (left) and conductivity  $\bar{D}$  (right) in cubic blocks from the experimental sample, for block sizes  $N_c = 16, 32, 64,$  and  $128$  (top to bottom). The vertical broken lines are the statistical averages.

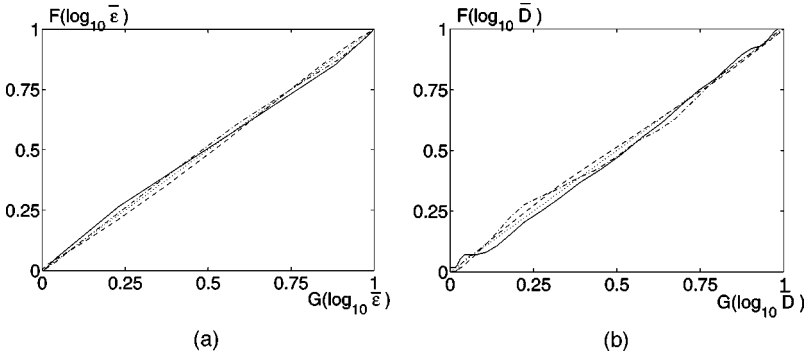


FIG. 9. Distribution functions of the logarithm of porosity (a) and conductivity (b) in cubic blocks with size  $N_c=32$  (—), 64 (- · - · -), and 128 (- - -) from the experimental sample, versus the Gaussian distribution function Eq. (26). Only percolating blocks are considered in (b), for  $N_c=32$ .

samples. When  $N_c$  increases, the number of blocks decreases and the overall statistical contents remain identical. Hence, the average porosity of the blocks,  $\langle \bar{\epsilon} \rangle$ , is of course a constant since it corresponds to the average  $\epsilon$  of the phase function  $Z$  over the same overall volume for all  $N_c$ .

The dispersion of the block porosities, quantified by the standard deviation  $\sigma_{\bar{\epsilon}}(N_c)$ , decreases with the block size  $N_c$ . For blocks large enough to sample all the variations of the local porosities,  $\sigma_{\bar{\epsilon}}(N_c)$  should decay as  $N_c^{-3/2}$ . However, a slower decay is observed for the data in Table II and Fig. 10, with an exponent  $-1.13$  (correlation coefficient  $r=0.9997$ , up to  $N_c=128$ ). This results from correlations between the porosities in the blocks. If one assumes that  $Z(\mathbf{r})$  is a stationary random correlated field, with a variance  $\sigma_Z^2 = \epsilon(1-\epsilon)$  and a spatial covariance  $C_Z = \sigma_Z^2 R_Z$ , the variance  $\sigma_{\bar{\epsilon}}^2$  is given by

$$\sigma_{\bar{\epsilon}}^2 = \frac{1}{\Omega^2} \int_{\Omega} d\mathbf{r}_1 \int_{\Omega} d\mathbf{r}_2 C_Z(\mathbf{r}_1 - \mathbf{r}_2). \quad (27)$$

TABLE II. Percolation and transport properties in cubic blocks of size  $L = N_c p_x$ , cut from the experimental and reconstructed samples. Brackets  $\langle \rangle$  denote averages over the blocks;  $\sigma_X$  is the standard deviation of  $X$ .

$N_c$	$L$ ( $\mu\text{m}$ )	$N_b$	$P_p$	$\langle \bar{\epsilon} \rangle$	$\sigma_{\bar{\epsilon}}$	$\langle \bar{\epsilon} \rangle_p$	$\langle \bar{D} \rangle$	$\sigma_{\bar{D}}$	$r_{\bar{\epsilon}, \bar{D}}$
512 <sup>3</sup> CMT image of the experimental sample									
16	101	32768	0.216	0.0692	0.0837	0.1641	0.0136	0.0436	0.758
32	202	4096	0.355	0.0692	0.0385	0.0943	0.0062	0.0151	0.683
64	403	512	0.580	0.0692	0.0166	0.0752	0.0027	0.0037	0.568
85	506	216	0.727	0.0692	0.0136	0.0714	0.0024	0.0025	0.552
128	806	64	0.875	0.0692	0.0080	0.0702	0.0019	0.0016	0.677
170	1070	27	0.960	0.0692	0.0075	0.0695	0.0020	0.0011	0.753
256	1610	8	1.000	0.0692	0.0053	0.0692	0.0018	0.0006	0.852
512 <sup>3</sup> Reconstructed sample									
16	101	32768	0.211	0.0697	0.0926	0.1859	0.0154	0.0456	0.772
32	202	4096	0.339	0.0697	0.0452	0.1064	0.0071	0.0154	0.699
64	403	512	0.564	0.0697	0.0195	0.0779	0.0034	0.0047	0.653
96	605	125	0.736	0.0697	0.0114	0.0722	0.0024	0.0024	0.633
128	806	64	0.891	0.0697	0.0069	0.0704	0.0022	0.0016	0.679
170	1070	27	0.963	0.0697	0.0045	0.0699	0.0019	0.0011	0.361
256	1610	8	1.000	0.0697	0.0025	0.0697	0.0016	0.0008	0.443

The double integral (27) can be numerically evaluated if  $C_Z$  is given. This was done for the isotropic exponential covariance in Eq. (25), and cubic domains  $\Omega$  (see Fig. 10). It appears that the asymptotic decay  $\sigma_{\bar{\epsilon}} \propto L^{-3/2}$  is reached only for very large domains, with  $L/\mathcal{L} > 20$ . For smaller sizes, the numerical data are in excellent concordance with the prediction of Eq. (27).

For  $N_c \geq 128$ , the decay rate of  $\sigma_{\bar{\epsilon}}$  should increase and reach the asymptotic regime  $\sigma_{\bar{\epsilon}} \propto L^{-3/2}$ . However, the statistical variability predicted by Eq. (27) for a stationary medium is dominated by the macroscopic variation of the porosity along the  $z$  direction shown in Fig. 5(c). Hence, the decay of  $\sigma_{\bar{\epsilon}}$  with  $N_c$  actually becomes slower, and  $\sigma_{\bar{\epsilon}}$  for  $N_c=256$  is 0.6%, i.e., roughly half the magnitude of the porosity step variation in Fig. 5(c).

It is also interesting to consider the spatial organization of the locally averaged porosities. To this end, we measured the spatial covariance  $C_{\bar{\epsilon}}$  of the local porosities  $\bar{\epsilon}$  in the  $N_c^3$  domains. This was done for various block sizes, ranging from  $N_c=16$  to 96. The results are plotted in Fig. 11(a), on

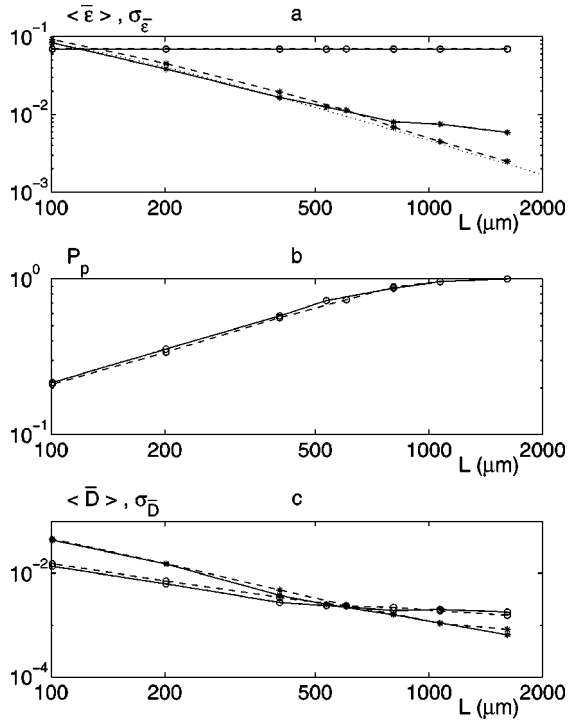


FIG. 10. Porosity  $\bar{\epsilon}$  (a), probability of percolation  $P_p$  (b) and conductivity  $\bar{D}$  along the  $x$  direction (c), versus the block size  $N_c$ . The symbols denote statistical averages ( $\circ$ ) and standard deviations (\*). Data are for the real (—) and reconstructed (---) samples. The dotted line is the prediction Eq. (27), for the isotropic exponential covariance in Eq. (25), and cubic domains  $\Omega$ .

average over the  $x$ ,  $y$ , and  $z$  directions.  $C_{\bar{\epsilon}}$  is remarkably insensitive to the block size, as soon as the lag exceeds 32 voxel sizes and  $N_c \geq 16$ . Furthermore, in this range, the porosity covariance is less than  $10^{-4}$ , which denotes the absence of any notable spatial organization of the porosity fluctuations. Even the variations along the  $z$  axis in Fig. 5c do not induce significant differences between the functions  $C_{\bar{\epsilon}}$  in this direction and in the orthogonal ones.

In summary, this block of Fontainebleau sandstone is very homogeneous. Local porosity fluctuations are totally accounted for by the expected statistical variability for a stationary medium, up to a scale of  $800 \mu\text{m}$ , i.e., about 5 typical grain diameters (see Sec. V B 4). Fluctuations on a larger scale are small and without definite spatial organization.

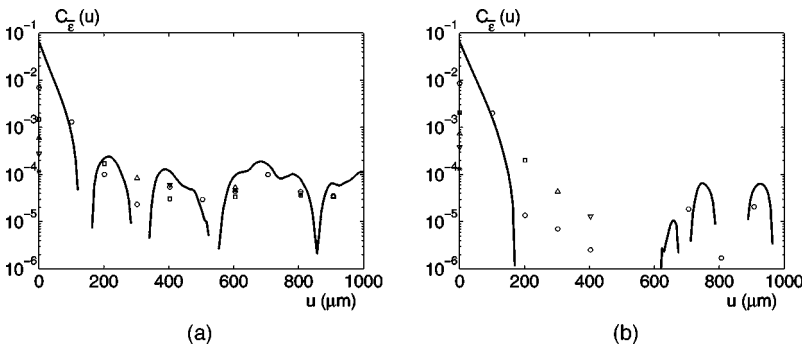


FIG. 11. Spatial covariance  $C_{\bar{\epsilon}}$  of the porosities measured in cubic blocks in the experimental (a) or reconstructed (b) samples, versus the lag in microns. The averaging domain size is  $N_c = 1$  (heavy line), 16 ( $\circ$ ), 32 ( $\square$ ), 48 ( $\triangle$ ), 64 ( $\nabla$ ) and 96 (\*).

TABLE III. Geometrical and topological parameters measured on the skeleton of the pore space in  $N=8$  blocks of size  $128^3$  voxels from the experimental and reconstructed samples. All distances are in microns. The volumetric quantities  $\bar{N}'_v$  and  $\beta'_1$  are in  $\text{mm}^{-3}$ .

	$\bar{N}'_v$	$\bar{z}$	$\beta'_1$	$\bar{r}_e$	$\bar{r}_v$	$\bar{d}_e$	$\bar{r}_M$	$C_{ee}$	$C_{ev}$	$C_{el}$
Exp	140	3.15	80	7.01	10.3	62.6	54.4	0.26	0.65	0.003
Rec	294	3.24	159	7.15	9.68	44.4	43.0	0.35	0.69	-0.008

### 3. Topology, skeleton and size distribution of the pore space

The skeleton of the pore space was extracted from eight  $128^3$  cubic blocks from the CMT image, as described in Sec. II C. Care was taken to avoid edge effects, by considering only the elements of the skeleton that are undisturbed by the boundaries. It was also checked that the block size is sufficient to obtain reliable results, by comparison with the corresponding results for smaller blocks.

The statistics for the characteristics of the components of the graph are given in Table III. Their distributions are presented in Fig. 12. Note that most edges have a critical radius  $r_e$  of the order of the voxel size  $p_x$ . It will be seen in Sec. V C 2 that the quasitotality of the pore space is connected in a single cluster. Thus, the resolution of the CMT scan is sufficient to preserve all the connectivity, but could not be much downgraded without losing connections.

Adjacent elements of the skeletons are weakly correlated; the coefficient  $C_{ee}$  for the radii of two edges with a common vertex is only 0.26; the radius and length of the vertices are statistically independent ( $C_{el} \approx 0$ ). The larger value of the correlation coefficient  $C_{ev}$  of the radii of an edge and of its end vertices probably results from the constraint that  $r_v \geq r_e$ .

### 4. Solid size distributions

The solid size distribution was measured in the  $512^3$  CMT image, as described in Sec. II B. The results are displayed in Fig. 13. Figure 13(a) is a  $256^2$  voxels cross section through the block, and Fig. 13(b) is the corresponding  $r_c$  field. Note that although this plot shows only a two-dimensional section,  $r_c$  was really determined in three dimensions. The histogram of  $r_c$  and its distribution function  $G$  in the three-dimensional sample are plotted in Figs. 13(c) and 13(d), respectively.

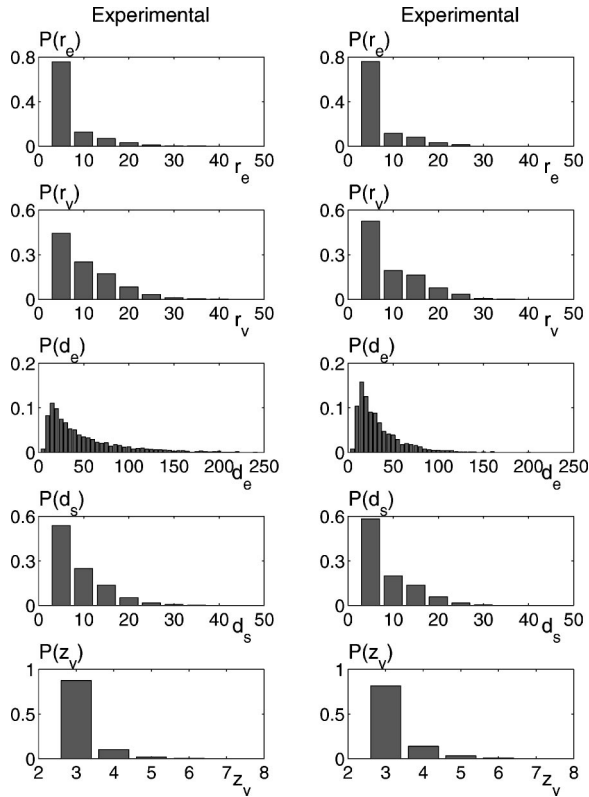


FIG. 12. Histograms of the critical edge radii  $r_e$ , vertex radii  $r_v$ , edge length  $d_e$ , distance to the solid surface  $d_s$ , and of the coordination number  $z_v$  in the skeletons of the pore space in  $N = 8$  blocks of size  $128^3$  voxels from the experimental (left) and reconstructed (right) samples. All distances are in microns.

Even though this property is not used in the reconstruction algorithm, it is interesting to note that the distribution of  $r_c$  in the solid phase (i.e., excluding  $r_c = 0$ ) is close to Gaussian.

### C. Percolation and conductivity

#### 1. Numerical simulations

Since currently available computers do not allow yet for the resolution of transport equations in the full sample volume (about 134 million voxels), the numerical investigations were conducted on cubic subsamples of varying sizes from the experimental three-dimensional images. These subsamples are the same as for the multiscale analysis of porosity in Sec. V B 2.

Percolation and conductivity were investigated, with  $N_c$  ranging from 16 to 256, which corresponds to cubes of dimensions 0.10–1.61 mm. The smallest dimension  $N_c p_x$  is still about four times larger than the correlation length  $\mathcal{L}$  given in Table I. The largest cubes correspond to 1/8 of the whole sample volume.

#### 2. Statistical averages

The first property to be determined for each block is its percolation status. Some of the blocks are not percolating, i.e., no continuous path exists across the blocks through the

pore space. The fraction  $P_p = N_p/N_b$  of percolating blocks is given in Table II and it is plotted versus the block size in Fig. 10.

$P_p$  depends on the block size. For very small blocks, the percolating character is a random variable, since the block size is comparable to the characteristic length scale of the microstructure ( $\mathcal{L}$  or  $\lambda$ ), and the blocks are not statistically representative. In the limiting case  $N_c = 1$ ,  $P_p$  is exactly equal to the porosity  $\epsilon$ . For very large  $N_c$ , the blocks are representative of the macroscopic properties of the rock, and they should all have the same percolation status, i.e.,  $P_p = 0$  or 1. A transition takes place between these two limiting cases; assuming that the material is macroscopically homogeneous, the value of  $N_c$  when  $P_p$  reaches its macroscopic limit is an estimate of the scale at which the macroscopic transport properties can be safely evaluated.

In the present case,  $P_p$  is a smoothly increasing function of  $N_c$ , and  $P_p = 1$  for  $N_c \geq 256$ . The sample is percolating on the large scale. Furthermore, the quasitotality of the pore space is accessible from the boundaries, as was directly checked by an invasion simulation on the  $512^3$  cubic sample. The volume fraction of closed porosity is less than  $6 \times 10^{-3}$ , and it may originate in part from an insufficient spatial resolution of the CMT scan.

Percolation with a porosity smaller than 0.07 is a remarkable feature, that many reconstruction procedures are unable to simulate. Recall for comparison that the percolation threshold in three dimensions is  $\epsilon_c \approx 0.31$  for uncorrelated site lattices and  $\epsilon_c \approx 0.11$  for homogeneous correlated media without long-range order. A strong spatial heterogeneity is required to lower  $\epsilon_c$  to 0.07, Ref. [31].

Note also the large sample size required to ensure a percolation probability close to unity, despite the fact that nearly all the pore space is connected.

The average porosity  $\langle \bar{\epsilon} \rangle_p$  measured only in the percolating samples is significantly larger than the overall average  $\epsilon$  for  $N_c = 16$  (0.164) and  $N_c = 32$  (0.094). The difference  $\langle \bar{\epsilon} \rangle_p - \epsilon$  rapidly vanishes for larger block sizes, and it is smaller than 0.002 as soon as  $N_c \geq 85$ .

The average  $\langle \bar{D} \rangle$  of the conductivity over all blocks (percolating or not) is given in Table II and Fig. 10, together with its standard deviation  $\sigma_{\bar{D}}$ . In all cases, it decreases with the block size  $N_c$ , but it roughly stabilizes at  $\langle \bar{D} \rangle \approx 0.002$  when  $N_c \geq 128$  (block size  $\geq 0.80$  mm). The decay rate of the standard deviation  $\sigma_{\bar{D}}$  with the averaging block size  $N_c$  is fairly constant and faster than for the porosity fluctuations  $\sigma_{\bar{\epsilon}}$  ( $\sigma_{\bar{D}} \propto N_c^{-1.54}$ ,  $r = 0.995$ , for  $N_c = 16$  to 256).

#### 3. Statistical distributions

The statistical distribution of the decimal logarithm of conductivity in individual blocks is displayed in Fig. 8, for various block sizes. Again, all the distributions become narrower when  $N_c$  increases, and just like porosity, conductivity is well described by a lognormal probability law, as shown by the plot of the distribution function of  $\ln(\bar{D})$  in Fig. 9(b), provided of course that the nonpercolating blocks are excluded from the statistical sample.

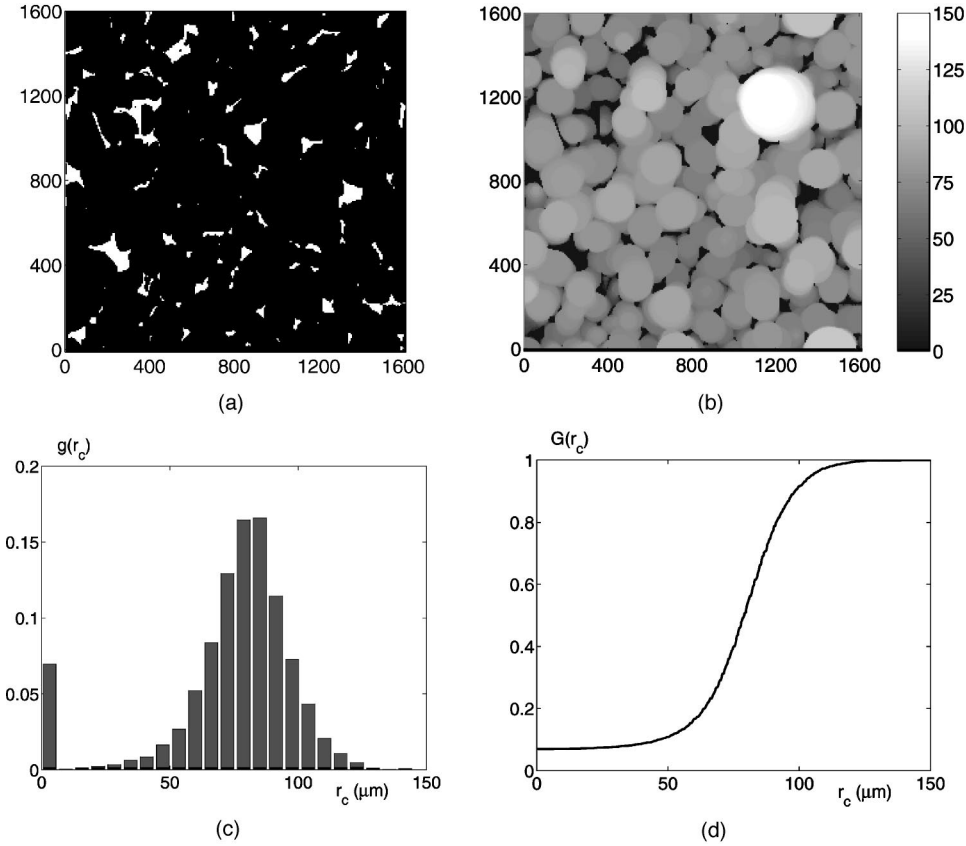


FIG. 13. Covering radius in the experimental sample. (a) is a  $256^2$  voxels section through the block and (b) the corresponding  $r_c$  field. The global histogram and distribution function of  $r_c$  are plotted in (c) and (d), respectively. All distances are in microns.

#### 4. Correlation between local porosity and conductivity

The conductivities of individual blocks are plotted versus the corresponding porosity in Fig. 14, in Cartesian (for all blocks) and logarithmic (for percolating blocks) coordinates.

Of course,  $\bar{D}$  is globally an increasing function of  $\bar{\epsilon}$ , but the data are very scattered. For small blocks ( $N_c = 16$ , block size =  $100 \mu\text{m}$ ), the data cover quasievenly the whole region between the two lines  $\bar{D} = 0$  and  $\bar{D} = \bar{\epsilon}$ , which correspond to the general Wiener's [32] bounds. When  $N_c$  increases, the range of observed porosities decreases. Simultaneously, the upper limit of the domain containing the data points lowers. Finally, for  $N_c = 128$  (sample size =  $800 \mu\text{m}$ ), the data are distributed between the two lines  $\bar{D} = 0$  and  $\bar{D} = \bar{\epsilon}^2$ .

The correlation coefficient  $r_{\bar{\epsilon}, \bar{D}}$  of the conductivity with the porosity of the blocks was evaluated (see Table II). It never reaches 0.9, which confirms the poor correlation of the local porosity and conductivity visible in Fig. 14.

## VI. ANALYSIS OF THE RECONSTRUCTED SAMPLE

### A. Reconstructed samples

The reconstruction procedure described in Sec. III has been applied, based on the geometrical characteristics measured on the real sample, namely, the global porosity and the solid size spectrum in Fig. 13. A numerical sample made up of  $512^3$  elementary cubes was produced. The elementary cube size corresponds to the voxel size  $p_x = 6.3 \mu\text{m}$  in the experimental CMT image. A three-dimensional view of the

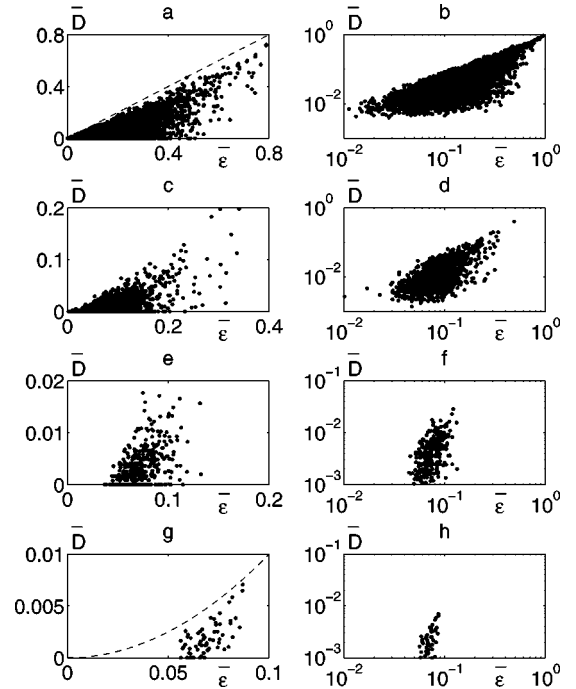


FIG. 14. Conductivity  $\bar{D}$  versus porosity  $\bar{\epsilon}$  in cubic blocks cut in the experimental sample, for block sizes  $N_c = 16, 32, 64,$  and  $128$  (top to bottom), in Cartesian (right) and logarithmic (left) coordinates. Broken lines correspond to  $\bar{\epsilon}$  in (a) and to  $\bar{\epsilon}^2$  in (g).

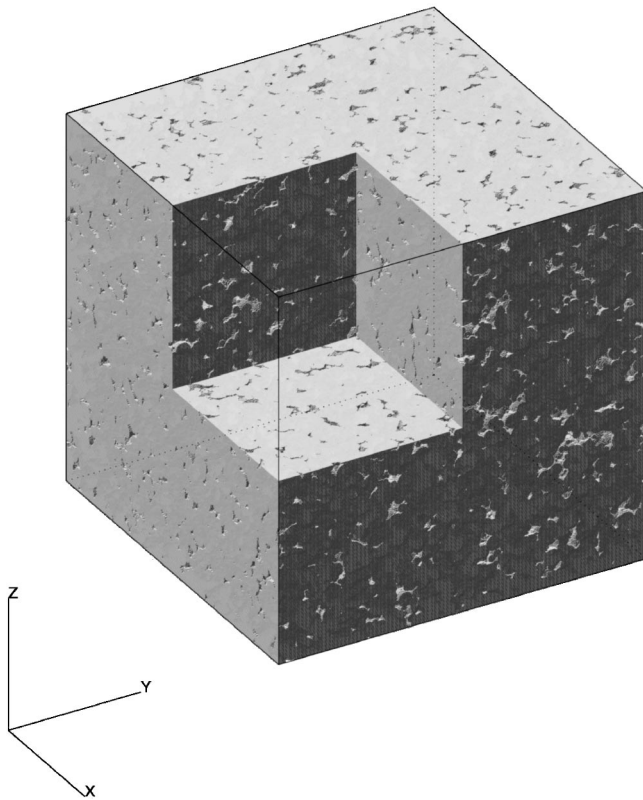


FIG. 15. Three-dimensional view of the reconstructed sample. The dimensions are  $512^3$  voxels, i.e.,  $(3.23 \text{ mm})^3$ .

reconstructed sample is provided in Fig. 15, which is in striking visual agreement with Fig. 1.

The geometrical and transport properties of the reconstructed sample were then investigated in the same way as in Sec. V for the real one.

## B. Geometrical characterization

### 1. Solid size distribution

The solid size distribution is the conditioning parameter for the reconstruction procedure, and thus, the covering radius spectra in the real and simulated materials are expected to be in good agreement. Figure 16 is the counterpart for the reconstructed sample of Fig. 13 for the experimental one. Figure 16(a) is a  $256^2$ -voxels cross section through the block, Fig. 16(b) is the corresponding  $r_c$  field, and Figs. 16(c) and 16(d) show the histogram and distribution function of  $r_c$ , respectively.

The general features of the histograms of  $r_c$  are indeed very similar, with the same balance of small and large radii. However, the histogram in Fig. 16(c) is slightly shifted towards larger radii. The curve for the distribution function in Fig. 16(d) is quasi-identical to the corresponding one in Fig. 13(d) within a translation of about one voxel size. This is probably due to discretization effects, and to the approximation mentioned in Sec. III, by which the possibility that a sphere surface is totally covered by smaller grains is ignored when deriving the sphere size distribution  $f(R)$  from the covering radius spectrum via Eq. (21).

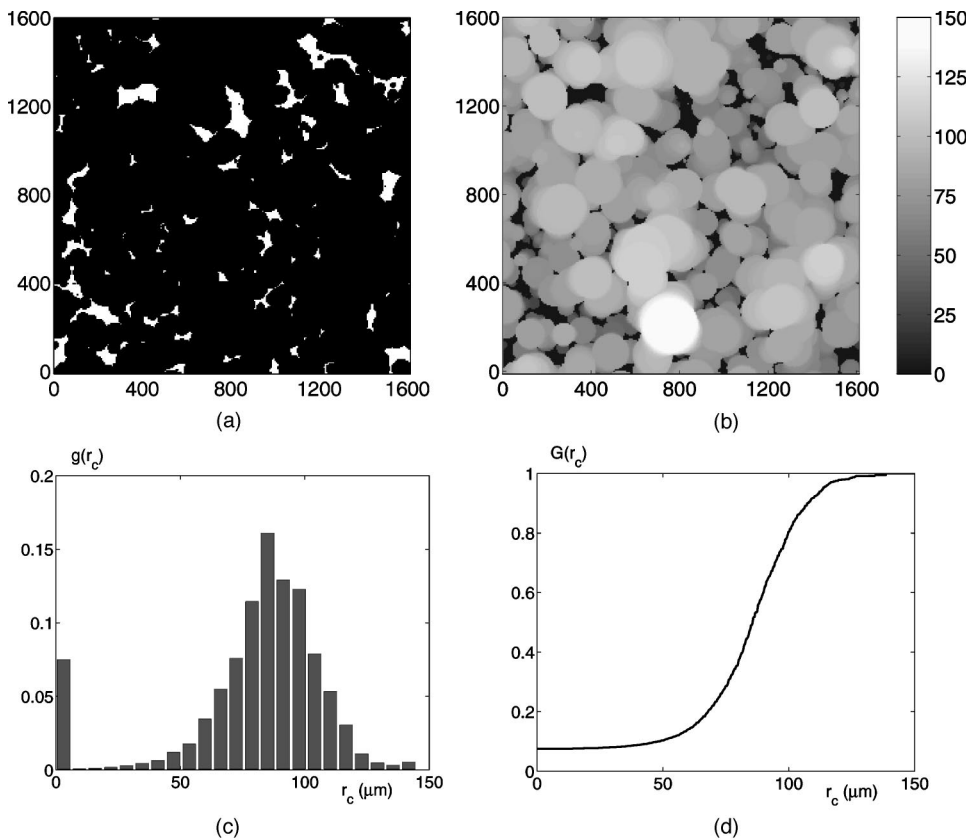


FIG. 16. Covering radius in the reconstructed sample. (a) is a  $256^2$  voxels section through the block and (b) the corresponding  $r_c$  field. The global histogram and distribution function of  $r_c$  are plotted in (c) and (d), respectively. All distances are in microns.

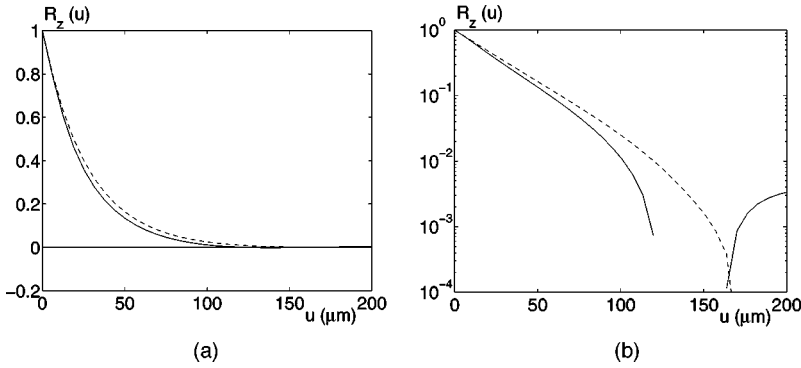


FIG. 17. Comparison of the correlation functions  $R_Z$  in the real (—) and reconstructed (---) samples. Linear (a) and semilogarithmic (b) coordinates. The lag is given in microns.

### 2. Global geometrical measurements

The porosity of the reconstructed sample is equal to 0.0697, i.e., it exceeds the prescribed value by  $2 \times 10^{-4}$ . This small difference is only due to statistical fluctuations.

The spatial correlations of the original and simulated media are compared in Fig. 17. They differ in two respects. First, the small anticorrelation observed in the real medium in the range 100–200  $\mu\text{m}$  does not exist in the reconstructed one, in agreement with Eq. (17), since there is no steric exclusion between the Poissonian spheres. Second, the decay of  $R_Z$  is slightly slower in the reconstructed sample. The semilogarithmic plot shows that the correlation is still exponential for lags up to 100  $\mu\text{m}$ , as given by Eq. (25), but with a decay length  $\lambda = 27.9 \mu\text{m}$ , i.e., 12% longer than in the real material, or about half a voxel size. This is a consequence of the shift of the covering radius spectrum mentioned in Sec. VI B 1. No long-range correlation exists in the reconstructed sample, since  $R_Z$  in Eq. (17) vanishes when the lag  $u$  exceeds twice the largest sphere radius.

### 3. Multiscale analysis, heterogeneity

Just like the experimental image, the reconstructed sample was split into cubic blocks, with size  $N_c^3$ . The standard deviations of the block porosities are given in Table II and plotted versus the block size in Fig. 10, in comparison with the measurements in the CMT image.

The comparison of the porosity standard deviation  $\sigma_{\bar{\epsilon}}$  is very good for block sizes up to 500  $\mu\text{m}$ , with an overestimate by about 15% in the reconstructed sample. This actually corresponds to the prediction of Eq. (27), with  $C_Z$  given by Eq. (25) and the larger value  $\lambda = 27.9 \mu\text{m}$ . For larger sizes,  $\sigma_{\bar{\epsilon}}$  in the reconstructed sample reaches the expected asymptotic regime ( $\sigma_{\bar{\epsilon}} \propto L^{-1.46}$ ,  $r = 0.9999$ , for  $N_c \geq 128$ ), since it does not contain any macroscopic features such as the porosity step in Fig. 5(c).

The spatial covariance  $C_{\bar{\epsilon}}$  of the local porosities is plotted in Fig. 11(b). It follows the same trends as the data for the experimental sample in Fig. 11(a).

The statistical distribution of the local porosities is very similar to that in the real sample, as shown by Fig. 18, to be compared to Fig. 8 for the real sample.

As a whole, the statistical geometrical properties of the real sample on a scale up to 800  $\mu\text{m}$  are well reproduced in the reconstructed one. The slight heterogeneity that could be detected on a larger scale was not accounted for in the re-

construction, and therefore, is absent in the numerical sample.

### 4. Topology, skeleton of the pore space

The pore-space skeleton was studied in the reconstructed sample and the results are compared with the data in the real one in Table III for the mean properties and in Fig. 12 for their statistical distributions.

Examples of skeletons in  $128^3$  blocks from the real and simulated media are compared in Fig. 19. They look similar on the large scale, in the sense that the skeletons do not penetrate in large regions of comparable extent. However, the skeleton in the reconstructed sample is more intricate on the small scale. Accordingly, the cyclomatic number in the simulated material is about twice that in the real sample. This

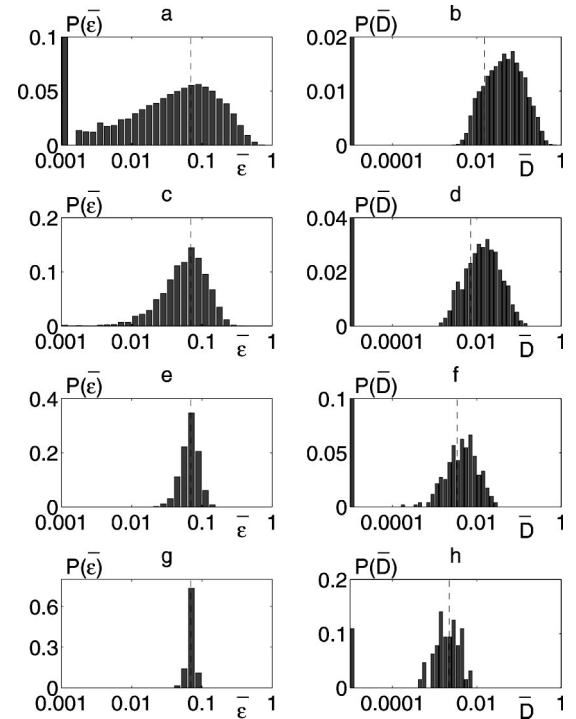


FIG. 18. Histograms of the decimal logarithms of the porosities (left) and conductivities (right) in cubic blocks from the reconstructed experimental sample, for block sizes  $N_c = 16, 32, 64,$  and  $128$  (top to bottom). The vertical broken lines are the statistical averages.

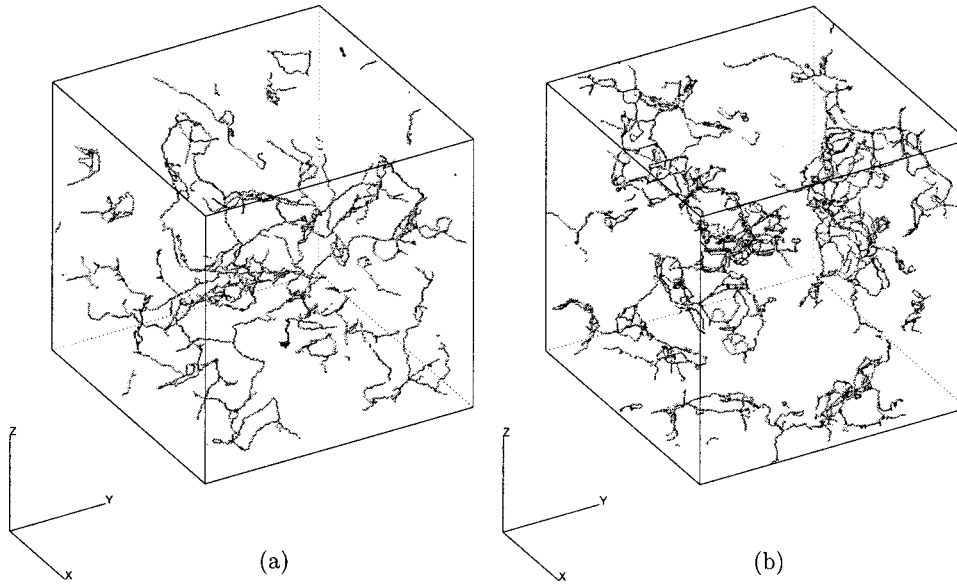


FIG. 19. Skeleton of the pore space in  $128^3$  blocks from the real (a) and reconstructed (b) samples.

results from a larger density  $N'_v$  of vertices, since the mean coordination numbers  $\bar{z}$  are nearly identical. The difference in the distributions of the edge lengths  $d_e$  confirms the visual observations. Many edges longer than  $150 \mu\text{m}$  exist in the real sample, which are totally absent in the reconstructed one. Conversely, the latter contains more very short edges, with  $d_e \sim 20 \mu\text{m} \sim 3p_x$ .

The mean edge and vertex radii,  $\bar{r}_e$  and  $\bar{r}_v$  are in perfect agreement with the same quantities in the real sample. Their histograms in both samples are also very similar. The difference in the radius  $r_M$  of the largest cavity is about  $10 \mu\text{m}$ , but it corresponds to a single event and has little statistical meaning. Finally, the correlations  $C_{ee}$ ,  $C_{ev}$  and  $C_{el}$  between the characteristics of the elements of the skeleton are quite similar to those in the real sample.

### C. Percolation and conductivity

The percolation status and conductivity coefficients of the blocks of various sizes in the reconstructed sample were computed as was done in the real sample in Sec. V C. The results are summarized in Table II, and they are plotted against the size  $N_c$  of the measuring volumes in Fig. 10. They are in striking concordance with the corresponding data for the real material.

Again, the sample is percolating on the large scale, as well as all the blocks with  $N_c \geq 256$ . The difference in percolation probability between the real and simulated media never exceeds 0.02, over the whole range of measuring domain size,  $N_c = 16$  to 512, i.e., 0.1 to 3 mm.

The average  $\langle \bar{D} \rangle$  and the standard deviation  $\sigma_{\bar{D}}$  of the block conductivities are also in excellent agreement with those in the real sample within a few percents over the whole range of  $N_c$ .

The correlation coefficient between local porosity and conductivity in the reconstructed sample is also given in Table II. The only difference with the real medium is a smaller correlation for the largest blocks ( $N_c = 256$ ). This

correlation in the real sample originated in the large scale variation in porosity, which is absent in the simulated medium.

The statistical distribution of the local conductivity and its relation to local porosity are also very similar to those in the real sample, as shown by Figs. 18 and 20, to be compared with Figs. 8 and 14 for the real sample.

## VII. CONCLUDING REMARKS

We have presented in this paper a statistical characterization of grainlike consolidated porous media, and a reconstruction procedure conditioned by the size distribution spectrum, without any adjustable parameter. These methods have been illustrated by an application to a low-porosity sandstone, and yielded good agreements for various geometrical and transport-related features.

Perhaps the most outstanding result is the ability of the model to produce percolating media for porosities as low as 0.07 (and 0.04, with the present size distribution), and to accurately render the size dependence of local percolation probability.

In addition, the geometrical parameters measured on the pore-space skeleton are also obtained, and the conduction properties agree with those in the real sample in all respects. For all measuring block sizes,  $N_c = 16$ –256, the average conductivities, their fluctuations and statistical distributions are in excellent concordance with their counterparts in the real material.

Other geometrical and transport properties, such as three- and four-point correlations and permeability, have not been tested here, but are systematically investigated in another study [25], where several reconstruction procedures, including the present one, are applied starting from CMT images of more porous and heterogeneous sandstones.

## ACKNOWLEDGMENT

Most computations were performed at CINES (subsidized by the MENESR) whose support is gratefully acknowledged.

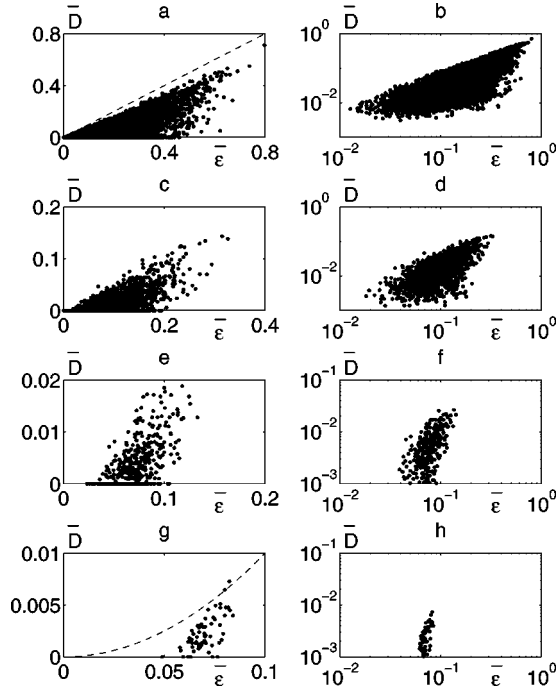


FIG. 20. Conductivity  $\bar{D}$  versus porosity  $\bar{\epsilon}$  in cubic blocks from the reconstructed sample, for block sizes  $N_c = 16, 32, 64,$  and  $128$  (top to bottom), in Cartesian (right) and logarithmic (left) coordinates. Broken lines correspond to  $\bar{\epsilon}$  in (a) and to  $\bar{\epsilon}^2$  in (g).

#### APPENDIX: DERIVATION OF THE SIZE DISTRIBUTION OF POISSONIAN SPHERES FROM THE TWO-POINT CORRELATIONS

The second derivative of  $\alpha$  can be obtained from Eq. (18b) as

$$\frac{d^2\alpha}{du^2} = -\frac{3u}{8\langle R^3 \rangle} \int_{u/2}^{+\infty} f(R) dR = -\frac{3u}{8\langle R^3 \rangle} \left[ 1 - F\left(\frac{u}{2}\right) \right]. \quad (\text{A1})$$

This directly yields the probability distribution  $F$  and density  $f$  of the sphere radii

$$F\left(\frac{u}{2}\right) = 1 + \frac{8\langle R^3 \rangle}{3u} \frac{d^2\alpha}{du^2}, \quad (\text{A2a})$$

$$f\left(\frac{u}{2}\right) = \frac{16}{3}\langle R^3 \rangle \frac{d}{du} \left[ \frac{1}{u} \frac{d^2\alpha}{du^2} \right]. \quad (\text{A2b})$$

Alternatively, the size distribution can be quantified by the volume-weighted density and distribution functions  $\mu_s$  and  $M_s$ . The density  $\mu_s$  is defined by

$$\mu_s(R) = \frac{R^3}{\langle R^3 \rangle} f(R). \quad (\text{A3})$$

Note that  $\mu_s$  differs from  $\mu$  in Eqs. (20) and (21) since the latter is the volume of spheres with radius  $R$  inserted per unit

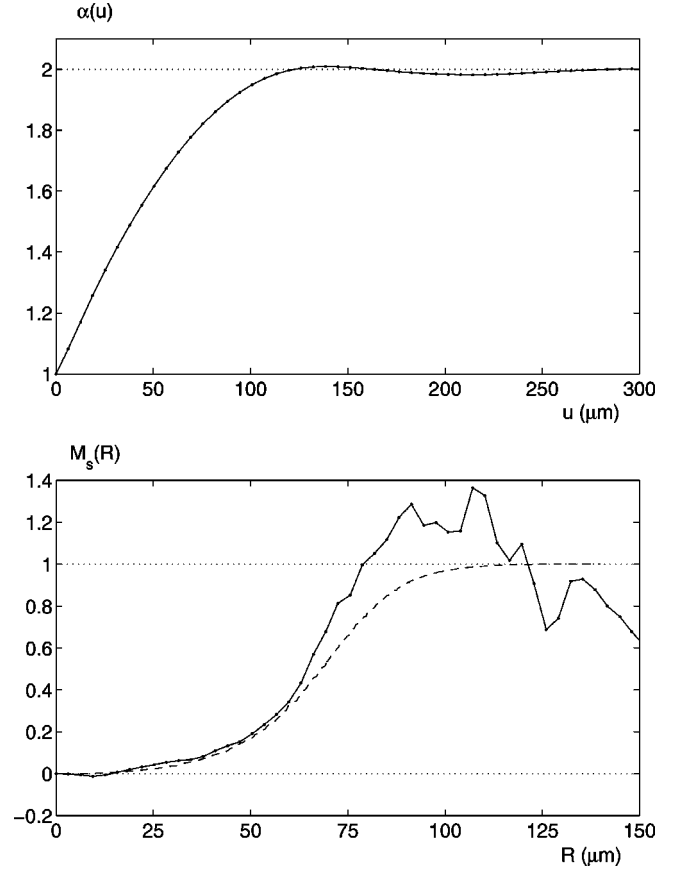


FIG. 21. The function  $\alpha$  measured on the experimental sample versus the lag  $u$ , and the sphere size distribution  $M_s$  derived from Eq. (A5b) versus the radius  $R$ . The broken line is  $M_s$  obtained from the measured distribution of covering radius  $r_c$  in Fig. 13.

total volume, whereas  $\mu_s(R)$  is measured per unit volume of inserted solid. They are related by

$$\mu(R) = -\ln \epsilon \mu_s(R). \quad (\text{A4})$$

Equations (A2b) and (A3) yield

$$\mu_s\left(\frac{u}{2}\right) = \frac{2}{3}u^3 \frac{d}{du} \left[ \frac{1}{u} \frac{d^2\alpha}{du^2} \right], \quad (\text{A5a})$$

$$M_s\left(\frac{u}{2}\right) = \frac{u^2}{3} \frac{d^2\alpha}{du^2} - u \frac{d\alpha}{du} + \alpha - 1. \quad (\text{A5b})$$

Equation (A5) gives the sphere size distribution that corresponds to a given two-point correlation function. In addition, Eqs. (A2b) and (A5a) provide the necessary and sufficient condition under which the function  $\alpha$  actually corresponds to Poissonian spheres, namely, that  $f$  or  $\mu_s$  are positive, i.e.,

$$\frac{d}{du} \left[ \frac{1}{u} \frac{d^2\alpha}{du^2} \right] \geq 0, \quad \text{for any lag } u. \quad (\text{A6})$$

Finally, the probability functions  $g$  and  $G$  of the covering radius can also be deduced from the correlations. In view of Eqs. (11) and (A4),

$$\begin{aligned} M_s(R) &= -\frac{1}{\ln \epsilon} \int_0^R \mu(r) dr \\ &= -\frac{1}{\ln \epsilon} [\ln G(r)]_0^R = 1 - \frac{\ln G(R)}{\ln \epsilon}. \end{aligned} \quad (\text{A7})$$

Therefore,

$$G(R) = \epsilon^{1-M_s(R)}. \quad (\text{A8})$$

The distribution  $M_s$  obtained by applying Eq. (A5b) to the

function  $\alpha$  deduced from the correlation measurements on the experimental sample is shown in Fig. 21. It compares fairly well with the distribution  $M_s$  derived from the measured distribution  $G(r_c)$  of the covering radius up to radii  $r_c \approx 60 \mu\text{m} \approx 10$  voxel size, even though the criterion (A6) is not satisfied for  $u \approx 15 \mu\text{m}$ . Beyond this range, the slight anticorrelation that peaks at  $u = 140 \mu\text{m}$  with  $\alpha = 2.0089$  ( $R_Z = -0.0017$ ) strongly affects  $M_s$ . Other tests without any anticorrelation (e.g., with the function  $\alpha$  measured on the reconstructed sample) have shown that  $M_s$  is also very sensitive to small statistical fluctuations of the long-range correlations. The erratic behavior of  $M_s$  for large radii is strongly amplified in  $G(r_c)$ , due to the small value of  $\epsilon$  in Eq. (A8).

- 
- [1] P.M. Adler and J.-F. Thovert, *Appl. Mech. Rev.* **51**, 537 (1998).
- [2] R.D. Hazlett, *Math. Geol.* **29**, 801 (1997).
- [3] C.L.Y. Yeong and S. Torquato, *Phys. Rev. E* **57**, 495 (1998).
- [4] C.L.Y. Yeong and S. Torquato, *Phys. Rev. E* **58**, 224 (1998).
- [5] C. Manwart and R. Hilfer, *Phys. Rev. E* **59**, 5596 (1999).
- [6] D. Coelho, J.-F. Thovert, and P.M. Adler, *Phys. Rev. E* **55**, 1959 (1997).
- [7] P.-E. Øren, S. Bakke, and O.J. Arntzen, *SPEJ* **3**, 324 (1998).
- [8] B. Biswal, C. Manwart, R. Hilfer, S. Bakke, and P.E. Øren, *Physica A* **273**, 452 (1999).
- [9] P.-E. Øren, S. Bakke, *Transp. Porous Media* (to be published).
- [10] R. Hilfer, *Adv. Chem. Phys.* **92**, 299 (1996).
- [11] B. Biswal, C. Manwart, and R. Hilfer, *Physica A* **255**, 221 (1998).
- [12] B. Biswal and R. Hilfer, *Physica A* **266**, 307 (1999).
- [13] G. Matheron, *Éléments pour une Théorie des Milieux Poreux* (Masson, Paris, 1967).
- [14] J. Serra, *Image Analysis and Mathematical Morphology* (Academic Press, London, 1982).
- [15] G.W. Horgan, *Eur. J. Soil. Sci.* **49**, 163 (1998).
- [16] B. Lu and S. Torquato, *Phys. Rev. A* **45**, 922 (1992).
- [17] J. Quintanilla and S. Torquato, *Phys. Rev. E* **54**, 4027 (1996).
- [18] J.-F. Thovert, J. Sallès, and P.M. Adler, *J. Microsc.* **170**, 65 (1993).
- [19] S. Bekri, K. Xu, F. Yousefian, P.M. Adler, J.-F. Thovert, J. Muller, K. Iden, A. Psyllos, A.K. Stubos, and M.A. Ioannidis, *J. Pet. Sci. Eng.* **25**, 107 (2000).
- [20] P. Hall, *Introduction to the Theory of Coverage Processes* (Wiley, New York, 1988).
- [21] J. Quintanilla and S. Torquato, *Phys. Rev. E* **55**, 1558 (1997).
- [22] J.G. Berryman, *J. Math. Phys.* **28**, 244 (1987).
- [23] C.A. Glasbey, G.W. Horgan, and J.F. Darbyshire, *J. Soil Sci.* **42**, 479 (1991).
- [24] G. Stell and P.A. Rikvold, *Int. J. Thermophys.* **7**, 863 (1986).
- [25] F. Yousefian, A. Ball, J.-F. Thovert, and P.M. Adler (unpublished).
- [26] P.M. Adler, *Porous Media: Geometry and Transports* (Butterworth/Heinemann, London, 1992).
- [27] V. Di Federico and S.P. Neuman, *Water Resour. Res.* **33**, 1075 (1997).
- [28] P.J. Reynolds, H.E. Stanley, and W. Klein, *Phys. Rev. B* **21**, 1223 (1980).
- [29] J.-F. Thovert, F. Wary, and P.M. Adler, *J. Appl. Phys.* **68**, 3872 (1990).
- [30] J.-F. Thovert, P. Spanne, C.G. Jacquin, and P.M. Adler, in *Proceedings of the 23rd EGS General Assembly, Nice, France, 1998* [*Ann. Geophys.* **16** (Suppl. I), C246 (1998)].
- [31] V.V. Mourzenko, J.-F. Thovert, and P.M. Adler, *Eur. Phys. J. B* **19**, 75 (2001).
- [32] O. Wiener, *Abh. d.K.S. Gesellsch. d. Wiss. Math.-Phys.* **32**, 509 (1912).